Three Photon Excited Image Scanning Microscopy for in-Depth Super-Resolution Studies of Biological Samples

Anton Classen,[1] I. Michel Antolovic,[2] Stanislav Vitha,[1] Mia Pacheco [1], Dylan McCreedy [1], Alexei V. Sokolov [1],
Girish S. Agarwal,[1] Aart J. Verhoef [1,*], and Alma Fernández [1,†]

[1]*Texas A&M University*, College Station, Texas 77843, USA

[2]*Pi Imaging Technology SA, CH-1015 Lausanne, Switzerland*

Multiphoton laser scanning microscopy is a powerful tool for deep imaging of thick biological samples. Image scanning microscopy (ISM) has demonstrated significant improvements in the signal-to-noise ratio in confocal laser scanning microscopy, while at the same time improving upon the effectively attainable resolution. Two-photon excitation (2PE), combined with ISM, has been shown to allow for deep tissue imaging with enhanced resolution compared to 2PE microscopy. Three-photon excitation (3PE) has enabled record imaging depth and contrast for multiphoton imaging, due to the superior suppression of out-of-focus signal generation. In this paper, we demonstrate super-resolution 3PE ISM. This is achieved using a single-photon avalanche detector array, and 1040-nm pulses for 3PE of blue fluorescence. This method enables subdiffraction limited resolution imaging of biological samples stained with blue fluorescent markers, such as mouse myocardial and spinal cord tissues stained with $4'$, 6-diamidino-2-phenylindole. Deconvolution improves the resolving power further and allows for imaging with better than $\lambda/8$ resolution with respect to the 3PE wavelength λ. With the ISM pixel reassignment procedure, we demonstrate a resolution enhancement of $\sim$1.6 laterally, compared to the resolution attained using a photomultiplier tube in a non-descanned detection arrangement, and a factor of $\sim$1.8 enhancement in axial resolution. The experimentally measured three-dimensional point spread function volume is shrunk $\sim$4.4-fold, which is close to the theoretically expected enhancement.

I. INTRODUCTION

Fluorescence microscopy has become one of the most powerful tools to look into biological processes and structures at the cellular and subcellular level. Fundamental limitations to the lower bound of the spatial resolution that can be achieved in conventional microscopes prompted the development of a variety of techniques that have enabled imaging resolutions below the diffraction limit [1–9]. Some of these techniques are now referred to as diffraction unlimited microscopy (or rather nanoscopy, as resolutions approaching 10 nm can be achieved [10]), and they make it possible to achieve an imaging resolution that is fundamentally unlimited by diffraction [1,3,4,9]. Other super-resolution techniques allow for a maximum resolution enhancement (up to twofold below the diffraction limit [2,5,9]). Those include computational and statistical fluctuation methods [11] such as super-resolution optical fluctuation imaging (SOFI) [5], super-resolution radial fluctuations (SRRF) [12], photobleaching microscopy

(PiMP) [13], as well as classical optics approaches such as structured illumination microscopy (SIM) [2] and image scanning microscopy (ISM) [6]. Note that additional resolution enhancement can be achieved by combining some of these methods (e.g., 2×2 when combining ISM and SOFI [14]) or through the use of nonlinearities [15]. Depending on the application, each of these groups of techniques offers advantages and disadvantages. Since SIM and ISM are based on principles of spatial frequency mixing in optical imaging and work with standard fluorophores, they offer reliable operation, and they provide resolution enhancement while maintaining high imaging speeds [16].

CLSM can in theory, with a very small pinhole, achieve the same resolution gain as ISM. When using a pinhole much smaller than the Airy disk, the full width at half-maximum (FWHM) of the resulting point spread function (PSF) $h_{\text{tot}}(\mathbf{r})$ is directly shrunk by $\sqrt{2}$ compared to the excitation PSF $h_{\text{exc}}(\mathbf{r})$ and can be further reduced by deconvolution, to achieve a factor 2. However, with this approach, the resolution enhancement comes at the cost of rejecting most signal light, leading to low signal-to-noise ratios (SNRs), and consequently worse resolutions in most practical cases. ISM overcomes this limitation by using a pixel array detector, where each pixel acts as an individual small pinhole. While the central pixel captures the "standard" super-resolving CLSM signal, the off-center pixels capture useful information that needs to be assigned to their correct positions in the image. This approach vastly

---

increases the SNR without sacrificing the $\sqrt{2}$ resolution enhancement.

The ISM approach was originally proposed in the 1980s [17,18], but only recent technological advancements made experimental implementations feasible. Different approaches were developed that digitally, optically, or optomechanically implement the required photon reassignment. In different demonstrations, these were termed image scanning microscopy [6], rescan confocal microscopy [19], optical photon reassignment microscopy [20], spot-scanning SIM [16], instant SIM (iSIM) [21], and they include parallelized versions with multibeam illuminations [22]. The optomechanical and optical solutions "rescan" the collected fluorescence or enlarge the image with a lens, respectively, to achieve the sought-after reassignment of the emitted fluorescence light. These techniques allow the use of a conventional camera, but they do not allow for further data postprocessing after collection. The ability to perform postprocessing, however, is an important feature for varying imaging conditions [23], for example when using fluorophores with different emission wavelengths. Straightforward and fast computational ISM solutions have only recently been enabled by fast detector arrays (with a response time at least as fast as the typical pixel dwell time of the focused laser beam) such as the AiryScan PMT array or with SPAD arrays such as the SPAD23 (23-elements, Pi Imaging Technologies) or the PRISM (25 elements, Genoa instruments) detectors.

Compared to single-photon excitation, multiphoton excitation restricts excitation axially, thereby reducing phototoxicity and out-of-focus photobleaching. This problem is also addressed by light-sheet microscopy [24], however requiring sample illumination from the side, thus placing restrictions on the sample geometry. Two-photon-excitation ISM (2PE-ISM) has also been proposed and successfully implemented to enable super-resolution imaging in thicker samples and scattering tissues that cannot be studied with 1PE alone [23,25,26]. The use of longer-wavelength excitation light bears several advantages, especially less scattering, reduced phototoxicity, and less absorption. While very deep tissue studies utilize non-descanned detection (NDD) to collect scattered and nonscattered fluorescence photons, intermediate regimes provide sufficient amounts of nonscattered ballistic photons, which are required to make use of the ISM principle in the detection pathway [23]. The confocality of the ISM principle also rejects a potentially strong near-surface (out-of-focus) fluorescence background signal which can be detrimental to NDD [23]. In this regard, it was shown that 2PE-ISM can provide a viable advantage for out-of-focus signal rejection. Moreover, 2PE-ISM provides higher resolution enhancement factors relative to multiphoton excitation with NDD compared to 1PE-ISM relative to standard confocal microscopy [27,28], and in a 2PE-ISM setup, the resolution of second-harmonic microscopy can be enhanced via ISM detection (SHG-ISM) [26].

Three-photon-excitation (3PE) microscopy has successfully allowed the demonstration of record optical imaging depths in biological tissues [29] as it provides superior suppression of out-of-focus signal background. Besides, it can equally provide a contrast mechanism complementary to 1PE and 2PE, and a laser source capable of providing 3PE contrast also allows us to provide contrast via 2PE (and 1PE). 3PE SIM has been demonstrated to achieve 106-nm lateral resolution, and 860-nm axial resolution [30]. While SIM typically achieves a slightly better lateral resolution and relies on wide-field detection and does not require laser scanning, ISM provides better optical sectioning [31] and requires laser scanning with descanned detection (which can be rescanned to allow detection on a camera sensor [25,26]). Enhancing the resolution, both laterally and axially, via 3PE-ISM can provide utility in instances where 1PE or 2PE do not provide the sought-after contrast mechanism, e.g., for the excitation of blue fluorescent molecules without the need to expose the sample to phototoxic ultraviolet (UV) and near-UV radiation and still have the ability to also detect far red emissions. It is worthwhile to note that adapting a conventional microscope for use with UV excitation may require more effort than adapting it for excitation with (near-)infrared sources commonly used in multiphoton microscopy. For example, the performance (transmission, aberrations, etc.) of many optical elements (especially lenses) degrades steeply for shorter (UV) wavelengths, thus requiring exchange with UV-optimized optics, while most standard microscope objectives perform well when used with near-infrared excitation. 3PE of blue or cyan fluorescent molecules can be naturally combined with simultaneous 2PE of orange or red fluorescent molecules, as well as second- and third-harmonic generation (which can highlight, respectively, collagen and lipid membranes label-free, for example) without the need for an additional laser source. Simultaneous 3PE of blue fluorophores and 2PE of red fluorophores also eliminates the need to sequentially record images taken with different wavelengths from a tunable laser.

Given the demonstrated power of SPAD array enabled ISM to improve the signal-to-noise ratio and enhance resolution in both CLSM and 2PE microscopy, we present here an experimental implementation of 3PE-ISM. We show the utility of this approach for various imaging scenarios, including multicolor imaging through the detection of the simultaneously generated 2PE signal of red fluorophores with 2PE-ISM. We achieve resolution enhancements of 1.7 in the lateral and 1.9 in the axial direction for 3PE-ISM over 3PE NDD. We demonstrate that with 3PE-ISM it is possible to surpass the resolution achievable with confocal microscopy for the same fluorophore, despite the three times longer excitation wavelength. Including deconvolution, the resolution enhancements reach factors of 2.5 in the lateral and 2.9 in the axial direction. This translates to a lateral resolution better than $\lambda/8$ respective to the wavelength of the excitation source. 3PE-ISM could be used as an alternative high-resolution imaging method for thick samples, especially with blue fluorophores for which deep blue or UV single-photon excitation might be inefficient due to lower transmission through optical components.

II. RESULTS

A. PSF benchmark samples

The results for imaging a sparse QD450 sample are shown in Fig. 1. The sample was first imaged with 3PE in a NDD configuration (top row in Fig. 1). We call this the "PMT" data set. Next, the sample fluorescence was descanned and focused
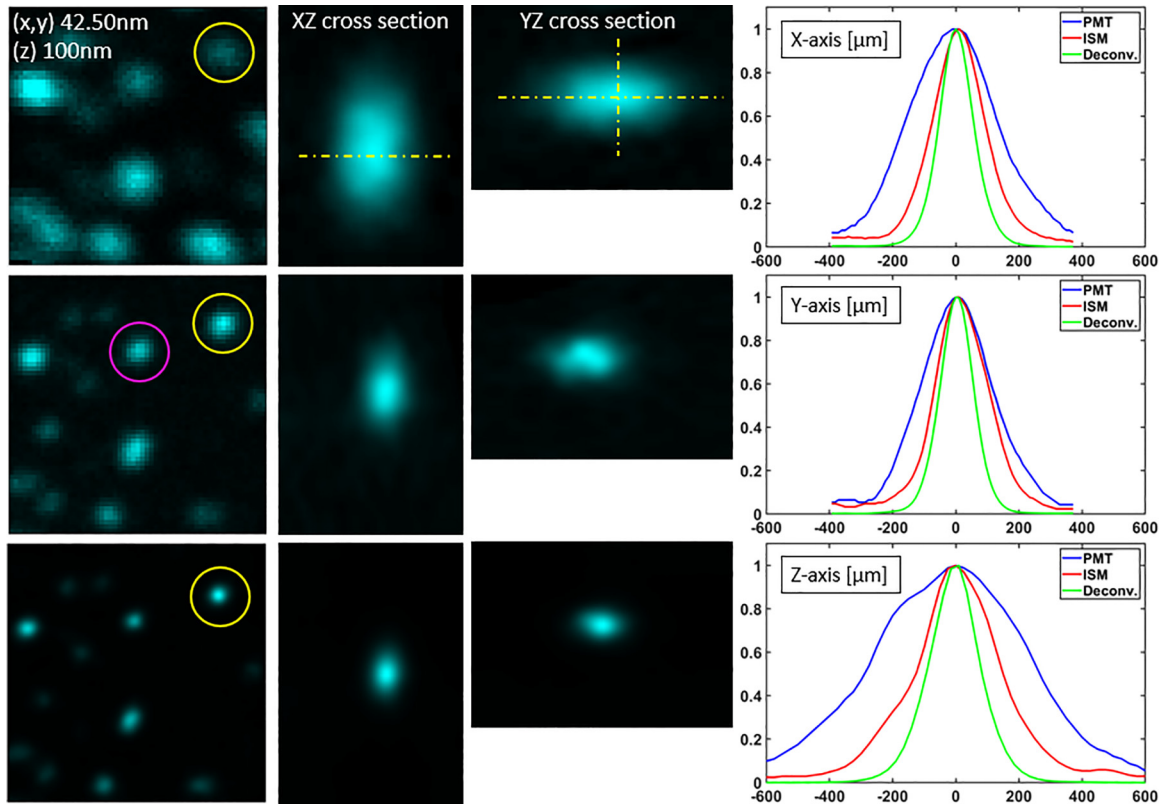
FIG. 1. Horizontal rows show (i) PMT, (ii) ISM, and (iii) DCV data sets. Vertical columns show (i) XY-slice, (ii) XZ view, (iii) YZ view, and (iv) line profiles along the x-, y-, and z-axes (see yellow dotted lines) of "spot 1" highlighted in the yellow circle. "Spot 2," which was used to produce Fig. 5, is highlighted in the magenta circle.

onto the SPAD array, with a total magnification of $M = 250$. The subimages from each SPAD pixel were postprocessed with our MATLAB ISM algorithm and then assembled into the final "ISM" image stack (middle row in Fig. 1). In addition, we applied RL deconvolution ("DCV" for short) to the ISM data set (bottom row in Fig. 1). Due to the blinking behavior of our quantum dots, individual spots may have different brightness in the two data sets. We applied interpolation and smoothing to all three data sets and displayed XZ and XY cross-sections of "spot 1" in Fig. 1, as this spot did not display blinking while acquiring the image stacks. Gaussian fits ($R^2 > 0.99$) of the corresponding line profiles yielded the following FWHM values (in nm):

axis:	x	y	z
PMT	317 ± 6	260 ± 4	551 ± 16
ISM	189 ± 2	187 ± 4	295 ± 10
DCV	128 ± 2	124 ± 2	188 ± 4

The 3PE-ISM data show a resolution enhancement of 1.68, 1.39, and 1.87 in the x, y, and z directions, respectively, compared to the NDD PMT data. Deconvolution further enhances the resolution over ISM by factor of 1.48, 1.51, and 1.57 (x, y, and z) and by a total of 2.47, 2.10, and 2.93 (x, y, and z) over the PMT data set. The resolution enhance-

ments along the axial direction stem from the confocality and out-of-focus light rejection of the descanned detection configuration. Along the x-axis, the enhancement matches the theoretically expected value of 68%. For the y-axis, a lower enhancement of 39% is obtained. We attribute this difference to the slightly elongated lateral (three-photon excitation) PSF profile, as revealed by the PMT measurements. Figure 1 of the Supplemental Material (SM) [32] shows images of quantum dot samples measured with orthogonal polarizations of the excitation source, indicating that the elongated excitation PSF we observe can be attributed to the tightly focused linear polarized excitation light [33]. Differences in asymmetries along the x, y, and z directions between different resolution-limited spots can be attributed to experimental noise, including blinking behavior of the quantum dots. Figure 2 of the SM [32] shows images from the same sample but with a larger field-of-view (FOV) to illustrate the ability of 3PE-ISM to maintain a constant resolution over a larger FOV and to facilitate additional measurements of the x and y profiles of more well-separated subdiffraction limited emission spots, which are shown in Fig. 3 of the SM [32].

B. Imaging of blue fluorescent biological samples

In a recent demonstration, we have investigated the utility of 3PE imaging as a complementary tool to confocal and 2PE imaging [34], especially when targeting blue fluorescent samples. To further enhance the utility of 3PE bioimaging, it is paramount to have resolution capabilities similar to
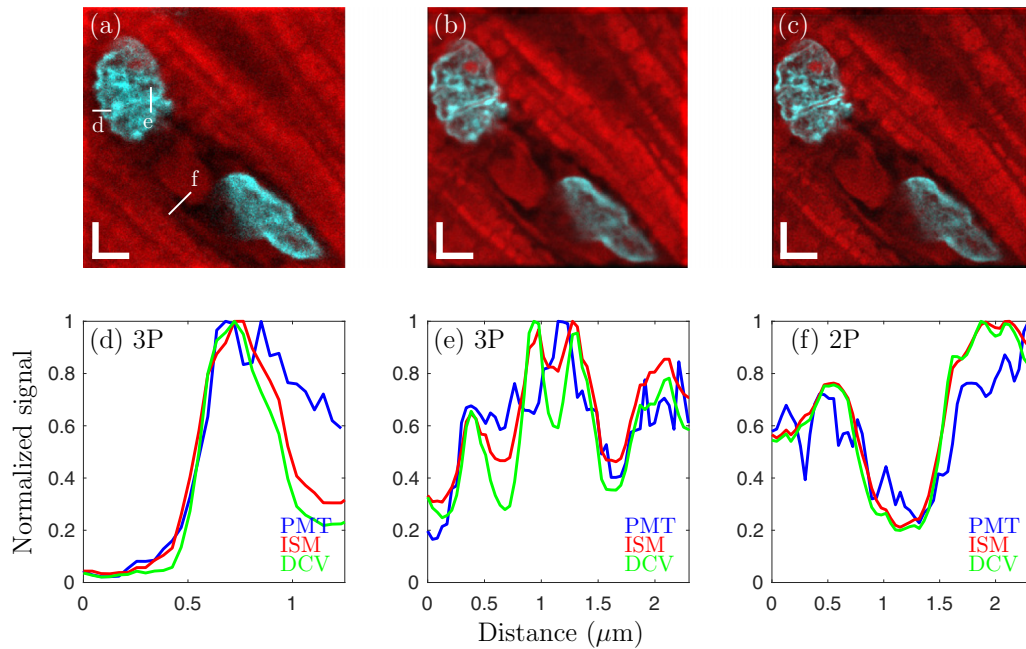
FIG. 2. 2PE and 3PE ISM imaging of fixed mouse myocardial tissue. Scale bars are 3 μm. Panels (a)–(c) show PMT, ISM, and DCV data sets, respectively, taken from this sample. Panels (d) and (e) show line profiles taken from the blue channel in the images taken at the positions indicated with "*d*" and "*e*" in panel (a), and panel (f) shows line profiles taken from the red channel at the position indicated with 'f' in panel (a). In (d)–(f) the red lines are taken from the PMT image, the blue lines from the ISM image, and the green lines from the DCV image, with the *x*-axis depicting the distance along the indicated white lines in panels (a).

confocal imaging, and to a lesser extent 2PE imaging. To achieve this goal, we showed 3PE-ISM imaging of blue fluorescence from biological samples with an excitation wavelength $\lambda = 1040$ nm. We chose samples that were stained with DAPI (see details under the Methods section). DAPI is a DNA stain and binds to sites in the cell nucleus of the biological tissue. With single-photon excitation, DAPI is most efficiently excited around 360 nm, close to one-third of our laser wavelength.

The first sample was fixed mouse myocardial tissue stained with DAPI mounted in a 80/20 glycerol/water medium and a refractive index of 1.44. The sample had a maximum thickness of 50 μm. We acquired a FOV of 21.76×21.76 μm on a 512×512 raster grid; see Fig. 2. The images show (a) PMT, (b) ISM, and (c) DCV data sets. While these samples generally do not seem to contain many sharp features, the resolution enhancement of ISM over PMT can be clearly observed. This is also aided by the higher contrast in the images stemming from the better axial resolution due to the confocality in the 3PE-ISM detection scheme. The resolution is then further enhanced by application of 10 iterations of an RL algorithm (DeconvolutionLab2 plugin). Final smoothing with a sharp Gaussian kernel reduces some of the high spatial frequency pixel noise. To illustrate the enhanced resolution and contrast, we have plotted three line profiles (normalized to the maximum value) indicated in panel (a). It can be seen that the ISM and DCV images capture more features of the DAPI DNA stain in the cell nucleus as well as in the red autofluorescence.

As the myocardial tissue is not cleared, it also serves to demonstrate imaging into scattering samples. Our sample had a maximum thickness slightly over 50 μm. Figure 2 of the

SM [32] shows PMT, ISM, and DCV data sets obtained near the bottom of the sample (about 50 μm deep). By evaluating the power needed to obtain the same signal strength across different depths using NDD, we estimate the scattering length for the 1040 nm excitation wavelength in this sample to be ~45 μm. By imaging the sample at 50 μm depth, we demonstrate the ability of 3P ISM to provide resolution enhancement despite high scattering losses of the signal.

To compare the resolution power of 3PE-ISM, we have imaged the same sample with a commercial Leica SP8 instrument, available at the Texas A&M University Microscopy and Imaging Center, as shown in Fig. 3 of the SM [32]. The sample was excited with a laser at $\lambda = 405$ nm and imaged with an index-matched glycerol immersion microscope objective (HC PL APO 63x/1.30 GLYC CORR CS2). The result for CLSM is shown in Fig. 2(d) of the SM [32]. The displayed FOV is 5.45×5.45 μm with 166×166 raster grid, resulting in a pixel pitch of 32.8 nm. These parameters were chosen automatically by the Leica LAS software suite (in Lightning mode) for best resolution measurements. The raw data were further deconvolved with the internal Lightning deconvolution algorithm. The final result is displayed in Fig. 1(e) of the SM [32]. Note that the Lightning deconvolution works on the full 3D stack, while we applied deconvolution only on a single 2D slice of the ISM data. The deconvolution results of the CLSM 3D data stack should therefore be inherently better. Nonetheless, it seems that the internal deconvolution algorithm may be overfitting features in the CLSM data set. Visually, the 3PE-ISM data and CLSM data set appear to have similar resolutions. PMT, ISM, and DCV DAPI images with a comparable FOV as the CSLM data are shown in Figs. 2(a)–2(c) of the SM [32]. While DAPI is routinely excited at 405 nm in CSLM
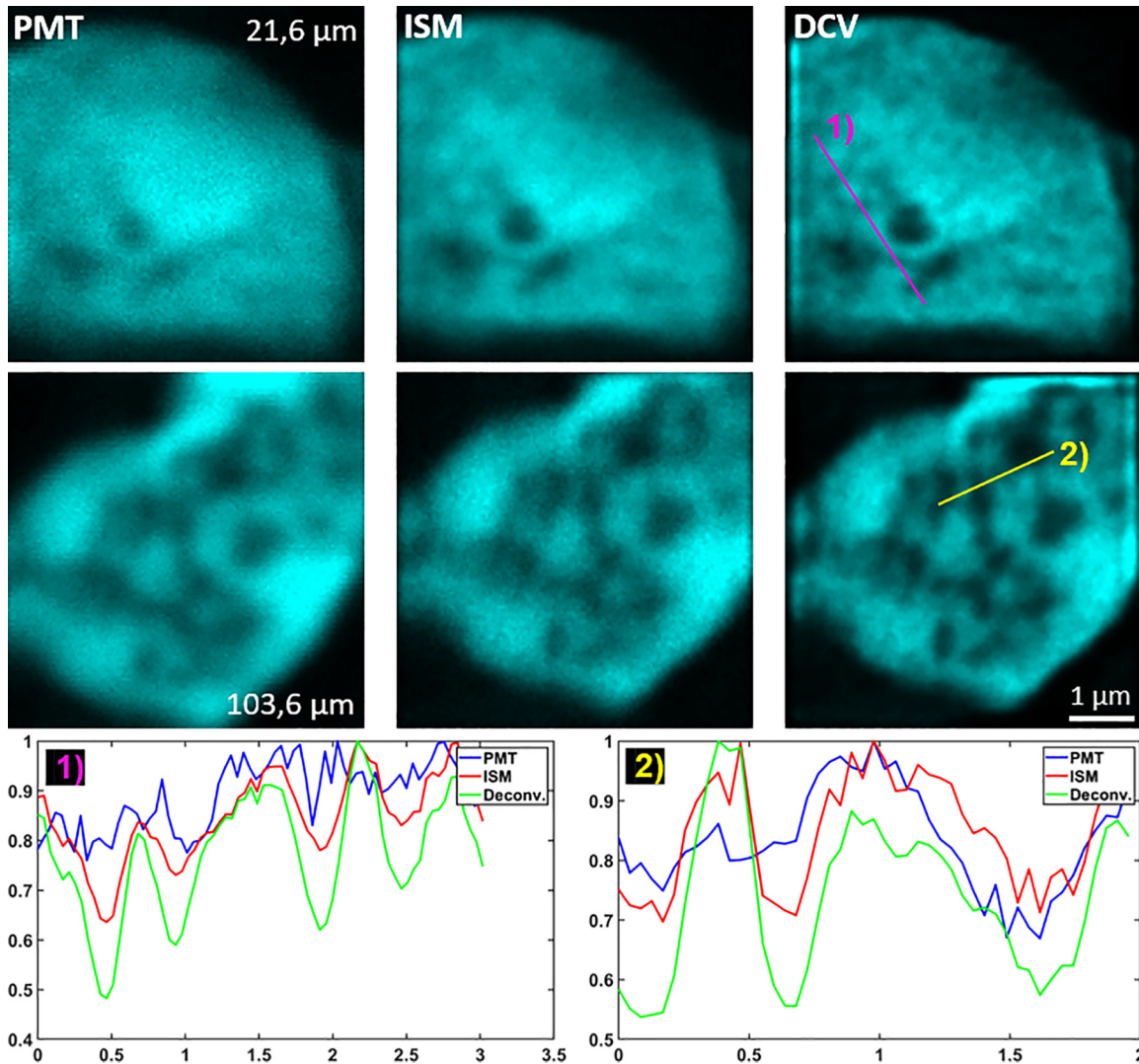
FIG. 3. Images of DAPI in spinal cord tissue, imaged at depths $z = 21.6\,\mu m$ (top row) and $z = 103.6\,\mu m$ (middle row). Left to right shows results for PMT, ISM, and DCV, respectively. Bottom row: line Profiles (i) and (ii) for PMT (blue), ISM (red), and DCV (green).

for quantitative imaging, we note that the raw CSLM images showed a noticeably stronger autofluorescence background than our 3PE images.

C. Diving deep with 3PE-ISM

We demonstrate the deep-tissue imaging capability with 3PE-ISM on a cleared mouse spinal cord sample. It is important to note that the clearing medium ethyl cinnamate is not exactly index-matched to F-type immersion oil. As a consequence, the actual imaging depth deviates from the "set" imaging depth—the distance the objective traveled down from the position where the top of the sample was in focus. This refractive index mismatch also causes increased spherical aberrations with increasing imaging depth. For example, the "set" imaging depth for the second row of images was 97 μm, and the actual depth of 103.6 μm is obtained using a simple calculation using trigonometrics and Snell's law for rays at half the angular acceptance of the objective, i.e., using the median ray approach proposed in [35].

Images at two different depths are displayed in Fig. 3, for 3PE-NDD with PMTs, for 3PE-ISM with the SPAD23 array, and additional RL deconvolution of the ISM image. It can be seen that the ISM approach enhances the resolution over NDD with a PMT throughout the sample. Deconvolution further enhances the resolution in this case, both at $z = 21.6\,\mu m$ and at $z = 103.6\,\mu m$ depth. This shows that a sufficient amount of ballistic photons reaches the SPAD23 array detector after descanning and refocusing the fluorescence light into a conjugate image plane, and that spherical aberrations are not limiting the imaging capabilities. Line profiles for the image at $z = 103.6\,\mu m$ are shown in the lower half in Fig. 3. These images clearly show superior contrast and resolution for the ISM and DCV images over the PMT image.

III. CONCLUSIONS

In this paper, we presented an experimental demonstration of super-resolution imaging via 3PE-ISM by detecting blue fluorescence generated in biological samples and QDs with
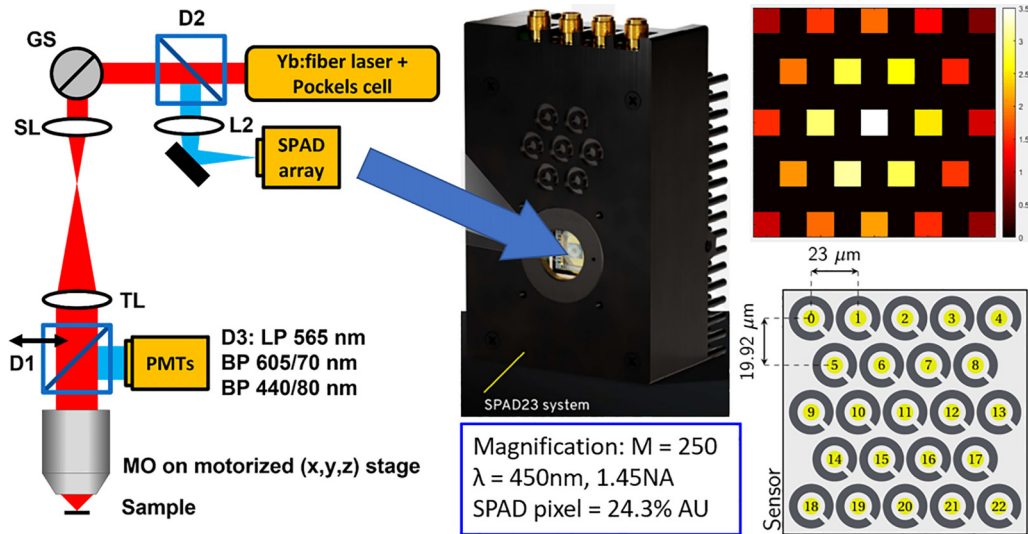
FIG. 4. Schematic illustration of the laser-scanning detection scheme, based on a customizable multiphoton microscopy platform (Sutter Instruments). The dichroic mirror D1 can be inserted or removed to enable non-descanned detection (NDD) with PMTs or detection with a SPAD array (SPAD23, Pi Imaging Technologies, middle column). The magnification at the conjugate image plane with SPAD array is $M = 250$, such that the 19 central pixels cover an area that corresponds to 1.25 AU. The top right image shows the photon distribution on the SPAD array when scanning over a bright and dense island of QD450 mounted on a cover slip. The detector is internally cooled, with the external heat exchanger visible on the back providing additional surface area to aid with heat dissipation.

a SPAD array. 3PE of blue fluorescent markers minimizes phototoxicity by eliminating the need for UV and near-UV excitation light. While the 3PE-ISM approach primarily enhances the lateral resolution, it also benefits from the confocal nature of the descanned detection, thus also boosting the effective axial resolution compared to non-de-scanned detection typically used in multiphoton microscopy. With the presented 3PE-ISM implementation we achieved a reduction of the 3D PSF by a factor of 4.4 compared to what is obtained with 3PE and NDD, and an additional factor of 3.5 reduction when RL deconvolution is applied. This corresponds to a total enhancement factor of 2.5 in the lateral direction and 2.9 in the axial direction. Compared to 3PE-SIM, 3PE-ISM provides more than fourfold improvement in axial resolution, as our diffraction-limited focusing provides a much stronger axial confinement than what is achieved with temporal focusing. In terms of the 3PE wavelength, the resulting lateral resolution can be expressed as $\lambda/8$. In absolute terms, we achieved a lateral resolution of 124 nm and an axial resolution of 187 nm with 3PE ISM combined with RL deconvolution.

The intrinsic optical sectioning of multiphoton microscopy approaches is of particular interest for *in vivo* imaging and imaging of thick samples. In this regard, 3PE-ISM also enhances the ability to obtain image stacks of thick samples while offering a resolution comparable to confocal approaches but with reduced risk of phototoxicity. The 3PE scheme with longer wavelengths and detection via ISM offers a good alternative for applications that involve excitation of fluorophores that require single-photon excitation wavelengths lying in the deep blue and UV spectral region, which suffers from low transmission and increased aberrations with conventional microscope optics, and consequently reduced image quality. In this work, we used a high-NA oil immersion objective with a maximum working distance of 130 μm, and we imaged

samples up to the maximum depth allowed by this objective. When using objectives with longer working distances, higher imaging penetration depths should be possible to achieve. Other advantages include the parallelization of light detection with a SPAD array, which enables a higher dynamic range compared to detection with a single element detector such as a PMT. Finally, when addressing fluorophores such as DAPI, 3PE using 1040 nm light allowed imaging of labeled cells with reduced autofluorescence in the blue detection channel compared to 405 nm CSLM.

This platform will also allow for combination with other super-resolution techniques, such as SOFI [5] and its quantum counter part, antibunching microscopy [7]. 1PE Q-SIM [36] and 1PE-SOFISM [14] have recently been demonstrated, both with a custom-built fiber bundle detector and with a SPAD array [37]. 3PE-ISM may also be demonstrated in a highly parallel version with multibeam illumination [38]. 3PE-ISM allows for imaging of significantly thicker samples with a resolution equal to or better than what can be achieved with standard CLSM.

IV. METHODS

A. Microscope setup

The equipment used for this work consists of a high-pulse-energy ultrafast fiber laser coupled to a customizable modular *in vivo* multiphoton microscopy system (MIMMS) [39]. A schematic illustration is shown in Fig. 4. The excitation laser source is an in-house-developed Yb:fiber chirped-pulse amplifier with a central wavelength of 1040 nm delivering energetic (μJ-level) sub-200-fs pulses [40]. These pulse parameters are well suited for two- and three-photon excitation microscopy schemes in general and for this project specifically. The pulse

repetition rate of the laser system can be tuned from kHz to 29 MHz [41,42] by integer-dividing the seed oscillator pulse frequency using a delay generator, or set to be equal to the oscillator repetition rate of 58 MHz. The excitation beam path contains two galvanometric scan (GS) mirrors (MDR, Sutter Instrument), the scan lens (SL, $f = 50$ mm), the tube lens (TL, $f = 200$ mm), and the microscope objective (Nikon MRD71970, 100×, 1.45 NA oil). The short working distance of the objective limits the imaging depth to 130 μm, however it is possible to achieve comparable results with longer working distance objectives [23]. The fluorescence detection path contains a removable long-pass dichroic beamsplitter (FF735-Di02-25 × 36, Semrock) for NDD with two photomultiplier tube (PMT) detector channels (H10770PA-40SEL, Hamamatsu), long-pass dichroic (T565lpxr, Chroma), and bandpass filters chosen from "blue" (ET440/80m-2p, Chroma), "green" (ET525/70m-2p, Chroma), and "red" (ET605/70m-2p, Chroma). The objective is mounted on a three-axis micromanipulator stage (MPC-200, Sutter Instrument) to position the objective over the sample and a piezoelectric stage (nPFocus 400, nPoint) to translate the focus axially with high precision. A half-wave plate before the microscope is used to control the polarization of the excitation beam.

The modularity of the MIMMS setup allowed adding a long-pass dichroic beamsplitter (D2) (ZT670rdc-xxrxt, Chroma) upstream of the scanning mirrors (GS). The lens L2 ($f = 125$ mm, AC254-125-B-ML, Thorlabs) focuses the fluorescence light into a conjugate image plane where the SPAD array (SPAD23, Pi Imaging Technologies) is placed. The total magnification on the SPAD array reads $M = 100 \times (125$ mm/50 mm$) = 250$, leading to a pixel size of 0.243 Airy units (AU) for each SPAD pixel, for fluorescence at $\lambda = 450$ nm. For 3PE-ISM studies a "blue" filter (ET440/80m-2p, Chroma) is mounted in front of the detector chip. The pixels are arranged in a hexagonal array, and consequently the distance from each pixel to all of its nearest neighbors is constant. Note that the filter range excludes any possible contributions from 2PE $\lambda_{\mathrm{em,2PE}} \geqslant 520$ nm or from third-harmonic generation (THG) at $\lambda_{\mathrm{THG}} = 1040$ nm/3 ≈ 347 nm.

In addition, a telescope consisting of two $f = 125$ mm lenses (AC254-125-B-ML, Thorlabs) was added upstream of D2 to enable axial translation of the excitation PSF ($\lambda = 1040$ nm) in the sample. Varying the distance of the two lenses creates a divergent or convergent beam on the galvo scan mirrors, and thus allows us to match the excitation PSF with the detection PSF when refractive index mismatches lead to a relative axial shift of the foci. The mismatch between $\lambda = 1040$ and 450 nm stems from the refractive index differences at these two wavelengths between the immersion oil (Leica, Type F), cover glass, and the sample mounting media utilized in this work (Mowiol, glycerol-water solution, or ethyl cinnamate).

B. Samples

In this work, we utilized different blue fluorescent benchmark and biological samples. The benchmark sample was used to assess the 3PE-ISM performance and the PSF. It was prepared by drop-casting a diluted solution of quantum

dots "QD450" [450 nm (CdSe/ZnS) quantum dots (HECZW), NNCrystal, size 7–8 nm] on a cover slip (170 μm thickness), air drying, and mounting the coverslip on a glass slide with Mowiol. The sparse quantum dot depositions are an ideal resolution test target due to their small size of 6–8 nm. Consequently, even for small clusters the feature size still remains far below the diffraction limit. The amount of QDs in a cluster can be estimated from its brightness compared to a dim spot that shows clear, "binary," fluorescence intermittence (i.e., blinking).

For bioimaging studies via 3PE-ISM, first we investigated a fixed mouse myocardial tissue mounted in a glycerol-water (80%/20%) medium. The sample was stained with the DNA stain DAPI in the cell nucleus and other dyes (e.g., AlexaFluor for microvasculature) in other parts of the cells.

The second bioimaging sample we tested was a 1-mm-thick murine spinal cord tissue cross-section, cleared using a modified iDISCO protocol [43], stained with DAPI, and embedded in ethyl cinnamate. This sample was utilized for deeper imaging studies, and we measured 2D slices at different positions and depths. Ethyl cinnamate possesses a refractive index >1.5 and is thus a good mounting medium for measurements with an oil immersion microscope objective. To mount small 1 mm sections of the spinal cord for imaging in an upright epifluorescence setup, we (i) placed a plastic washer (1 mm thick, 5 mm inner diameter) on a glass slide and fixed it with super glue (Loctite, standard store brand), (ii) coated the upper rim of the washer with super glue, (iii) placed the sample inside the washer and filled the "well" with a sufficient amount of ethyl cinnamate, and (iv) sealed the "well" with a standard 170 μm glass cover slip. We prepared multiple samples with this procedure and could reproducibly observe that the surface of the spinal cord samples was sitting at or just under cover slip. This enabled us to image deep into the sample, up to the maximum working distance of 130 μm provided by the oil immersion objective.

Note that studying the applicability of 3PE and 3PE-ISM microscopy in biological or microbial samples is of interest as a complementary technique to 2PE and confocal microscopy, and that the 3PE absorption cross-section spectrum is not simply the 1PE or 2PE absorption spectrum scaled to $\lambda/2$ or $\lambda/3$. As such, depending on the fluorophores used, with a single laser source, imaging in more than two well-separated color channels (e.g., blue, green and red instead of only blue and red) can also be achieved [34].

C. Pixel reassignment

The basis of ISM [6] is the full use of the excitation and detection PSF, $h_{\mathrm{exc}}(\mathbf{r})$ and $h_{\mathrm{det}}(\mathbf{r})$, respectively. For 2PE or 3PE the excitation PSF reads $h_{\mathrm{exc}}(\mathbf{r}) = [2J_1(\mathbf{r})/r]^2$ and $h_{\mathrm{exc}}(\mathbf{r}) = [2J_1(\mathbf{r})/r]^3$, yet the longer excitation wavelength leads to an initially reduced resolution power over 1PE. The SPAD array pixels in image space at geometric positions $\mathbf{s}_j$ ($j = 1, \ldots, 23$) measure the intensities $I_j(\mathbf{r}_i)$ at each raster-scan position $\mathbf{r}_i$ of the focused laser beam in the object space. A 2D image is obtained by raster scan positions $\mathbf{r}_i$ of 64×64, 128×128, 256×256, …"pixels." For the calculations, we demagnify the image plane coordinates $\mathbf{s} \equiv \mathbf{s}/M$ to match the scale of the object space coordinates $\mathbf{r}$. The PSF for each pixel
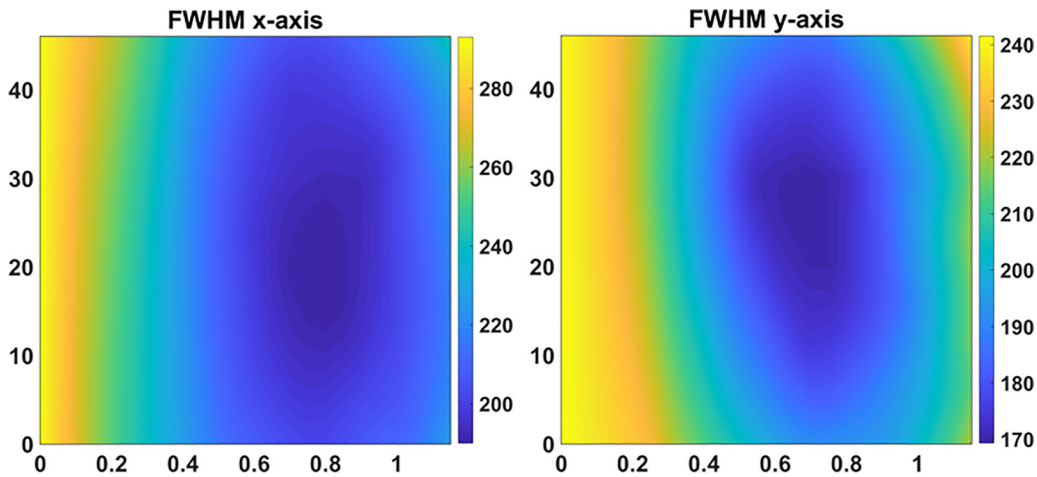
FIG. 5. Results of FWHM of a 2D Gaussian fit, applied to "spot 2" in the QD benchmark sample, in slice 8 of the *z*-stack; see Fig. 1. The plot show FWHM along the *x*-axis and along the *y*-axis. The displayed range of values covers $[0°, 46°] \times [0.00, 1.15]$. The geometric reassignment with the ideal value seems optimal; it is, however, not very sensitive around that value. The iterative reassignment does not perform better (FWHM not shown).

is effectively given by the product [23]

$$h_j(\mathbf{r}) = h_{\text{exc}}(\mathbf{r}) \times [p_j(\mathbf{r}) * h_{\text{det}}(\mathbf{r} - \mathbf{s}_j)], \qquad (1)$$

where the detection PSF is convolved with the area of the pixel $p_j(\mathbf{r})$ which forms a virtual pinhole. For a sufficiently small pixel, the effect of convolution with the area $p_j(r)$ is negligible, thus yielding the product of the excitation and detection PSF, and the signal at each pixel becomes

$$I_j = \int dr' h_j(r - r')I(r'). \qquad (2)$$

To obtain the ISM signal, a photon reassignment shift has to be applied, leading to [6]

$$I_{\text{ISM}}(\mathbf{r}) = \sum_{j=1}^{23} I_j(\mathbf{r} - \alpha \, \mathbf{s}_j), \qquad (3)$$

with the reassignment factor α. For 1PE without a fluorescence Stokes shift, the ideal value reads $\alpha = 0.50$, while for 3PE it reads $\alpha = 0.75$. A fluorescence Stokes shift reduces the value of α as it broadens the detection PSF compared to $\lambda = 1040$ nm/3 $= 347$ nm. The shift can be implemented on entire 2D subimages $I_j(\mathbf{r})$ at once, since the relative offsets $\mathbf{s}_j$ remain identical for each laser scan position $\mathbf{r}_i$. In this work, we utilized static reassignment vectors, calculated from the given geometry and magnification of the setup and optimized on data from the QD450 benchmark sample. It was found that $\alpha = 0.70$ was ideal for 3PE blue fluorescence from the QD450 sample (for 2PE we found $\alpha = 0.65$ as the optimal value). The shift vector matrix requires an additional rotation of 22° due to the tilted geometrical arrangement of the scanning mirror system. The ISM shifts have been implemented in a custom-written MATLAB script.

To account for any potential experimental imperfections or misalignments, we used the recorded data and iterated the reassignment procedure and FWHM measurements for a broad range of rotations from 0° to 46° and reassignment factors α from 0 to 1.15. As can be seen in Fig. 5, the expected values (22° and $\alpha = 0.70$) were confirmed, yet a broader range in the vicinity produced good results. Deviations of a few percent from the ideal value appear not to visibly alter the final

results. We have also implemented a similar "adaptive photon reassignment" approach as described by Koho *et al.* [23] via the automated image registrations procedure (imregister) in MATLAB, which aligns the 23 subimages of each SPAD pixel with the central pixel. While this procedure performed well, it did not outperform the iterative geometrical reassignment outlined above. It may be noted that especially for low SNR values the adaptive approach struggles, as excess noise causes it to be unable to reliably identify the correct similarities in the subimages.

It is of technical interest to note that subpixel image translations were implemented after conversion of the images from integer numbers that result from the photon-counting detector to floating point numbers. This avoids integer rounding errors, especially when a single-photon count is distributed across up to four pixels through bilinear interpolation upon pixel reassignment. For the PSF measurements, the images were also resampled on a finer grid through fourfold Fourier interpolation, which fully preserves the original image content but allows for a smoother visualization of the sharp 3PE-ISM PSF.

D. Simulations

To verify the full resolution enhancement potential of 3PE-ISM, we conducted simulations for 3PE with $\lambda = 1040$ nm in the excitation pathway, and 1PE with $\lambda = 450$ nm in the detection pathway. In both cases, the base PSF was assumed as the Airy disk $[2J_1(\mathbf{r})/r]$. For the numerical apertures we utilized experimentally derived FWHM values of the PSFs when imaging the QD450 sample. For the excitation PSF, we used the extracted FWHM values from 3PE laser-scanning microscopy. An average result around FWHM = 280 nm was found, which corresponds to an effective NA around 1.10 for the excitation pathway. For the detection PSF we benchmarked the microscope objective in a Leica DM6 wide-field microscope and in a Nikon AXR confocal microscope. In the wide-field microscope the available NA was extracted from the detection PSF with $\lambda = 450$ nm. In the confocal microscope the NA was determined with respect to the excitation
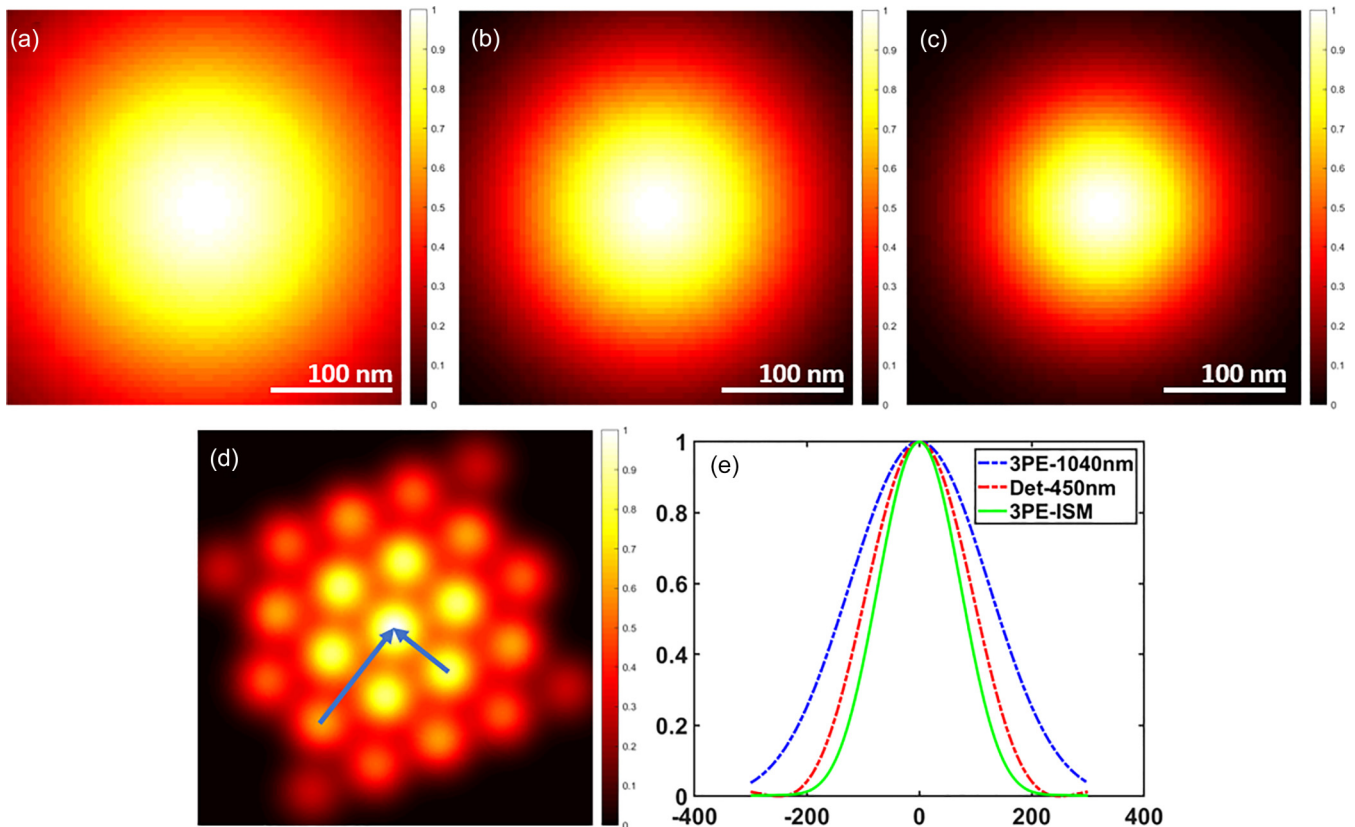
FIG. 6. Simulated PSFs for numerical aperture of 1.10 NA in the excitation and 1.15 NA in the detection pathway, respectively, showing (a) excitation PSF, 3PE with 1040 nm, (b) detection PSF, 1PE with 450 nm, and (c) 3PE-ISM PSF measured with SPAD23 array. (d) The PSF signals for all 23 detector pixels, separated by $3\,\mathbf{s}_j$ for visualization purposes. For the ISM technique, the signals are shifted as illustrated by blue arrows. (e) Lateral (normalized) PSF cross sections.

laser light at $\lambda = 405$ nm. In both cases, the extracted FWHM values correspond to approximately 1.15 NA for the detection wavelength. Performing this test with both a commercial Leica and Nikon system allows us to confirm that no significant deteriorations are caused by the use of the Leica scan lens in our multiphoton microscope system, as the objective performs equally well in both systems.

For the beam magnification we assumed $M_{\text{tot}} = 250$, leading to the pixel size diameter of 24.3 % of 1 AU ($\lambda = 450$ nm). In this geometry, the central 19 pixels of the SPAD23 array are located within 1.25 Airy units (Airy disk for $\lambda = 450$ nm, 1.45 NA). The subimages from each pixel [see Fig. 6(d)] are shifted toward the center (see blue arrows) with reassignment factor $\alpha\,\mathbf{s}_j = 0.70\,\mathbf{s}_j$. The simulations were implemented in a custom-written MATLAB script on a fine numerical grid, with numerical multiplications and convolutions of the excitation PSF, detection PSF, and pinhole in real space. We obtained FWHM values of 286, 211, and 169 nm, respectively, for the excitation, detection, and ISM PSF. The resolution of 3PE-ISM is enhanced by a factor of 1.68 over 3PE in a NDD configuration (see Fig. 6).

F. Deconvolution

SIM and ISM typically utilize a deconvolution process to amplify high spatial frequency information and to better approximate the sample's true structure, given the measured data. SIM often utilizes a generalized Wiener filter during assembly of all spatial frequency components. In ISM or 2PE-ISM, one can either use a Wiener filter or a maximum likelihood estimator, such as the Richardson Lucy (RL) algorithm. The latter performs better for noisy data and at removal of background. We opted for the RL algorithm, as implemented in the "DeconvolutionLab2" plugin [44] in FIJI. To deconvolve the QD450 data set, we utilized the z-stack of "spot 1" as the 3D PSF of our 3PE-ISM approach. The same PSF was also utilized for deconvolution of DAPI data sets from the two different samples. To avoid overfitting of noisy features and warp the image contents, we limited the RL algorithm to 10 iterations. PMT data (not shown) were deconvolved with the 3P PSF extracted from "spot 1" in the QD450 PMT data set. A blind deconvolution approach may also be utilized in following studies to not be reliant on an experimentally estimated PSF, and a regularization term can be used to allow for more iterations without warping the image content. Note that floating point images were transformed to integer values before application of the deconvolution algorithm, which expects Poisson sampling noise in the data sets.

The raw 3PE PMT and ISM data sets have been recorded with a pixel pitch of 42.5 nm in the lateral direction and a z-stack pitch of 100 nm. These values readily fulfill Nyquist sampling for the anticipated 3PE-ISM resolution. For easier visualization, we have smoothed the data sets in postprocessing. For the QD450 data sets we have applied a fourfold

Fourier interpolation along the *x*- and *y*-axes, including low-pass denoising in Fourier space to cut out high spatial frequency pixel noise that lies outside of the OTF support. In a second step we have applied a fourfold bicubic interpolation along the *z*-axis to obtain the 3D voxel size of 11.25 nm × 11.25 nm × 25.00 nm. The final resolution was estimated through FWHM analysis of single spots in the QD450 sample data sets. For DAPI data sets we have not applied further smoothing, as the feature sizes in these samples were less sharp. To remove some high spatial frequency pixel noise, we applied a convolution in real space with a sharp Gaussian kernel (amplitudes: 100%, 13.5%, 1.8% for the central pixel, direct neighbors, diagonal neighbors).

[1] S. W. Hell and J. Wichmann, Breaking the diffraction resolution limit by stimulated emission: stimulated-emission-depletion fluorescence microscopy, Opt. Lett. **19**, 780 (1994).

[2] M. G. L. Gustafsson, Surpassing the lateral resolution limit by a factor of two using structured illumination microscopy, J. Microsc. **198**, 82 (2000).

[3] E. Betzig, G. H. Patterson, R. Sougrat, O. W. Lindwasser, S. Olenych, J. S. Bonifacino, M. W. Davidson, J. Lippincott-Schwartz, and H. F. Hess, Imaging intracellular fluorescent proteins at nanometer resolution, Science **313**, 1642 (2006).

[4] M. J. Rust, M. Bates, and X. Zhuang, Sub-diffraction-limit imaging by stochastic optical reconstruction microscopy (storm), Nat. Methods **3**, 793 (2006).

[5] T. Dertinger, R. Colyer, G. Iyer, S. Weiss, and J. Enderlein, Fast, background-free, 3D super-resolution optical fluctuation imaging (SOFI), Proc. Natl. Acad. Sci. USA **106**, 22287 (2009).

[6] C. B. Müller and J. Enderlein, Image scanning microscopy, Phys. Rev. Lett. **104**, 198101 (2010).

[7] O. Schwartz, J. M. Levitt, R. Tenne, S. Itzhakov, Z. Deutsch, and D. Oron, Superresolution microscopy with quantum emitters, Nano Lett. **13**, 5832 (2013).

[8] S. Culley, K. L. Tosheva, P. Matos Pereira, and R. Henriques, Srrf: Universal live-cell super-resolution microscopy, Int. J. Biochem. Cell Biol. **101**, 74 (2018).

[9] L. Schermelleh, A. Ferrand, T. Huser, C. Eggeling, M. Sauer, O. Biehlmaier, and G. P. C. Drummen, Super-resolution microscopy demystified, Nat. Cell Biol. **21**, 72 (2019).

[10] F. Huang, G. Sirinakis, E. S. Allgeyer, L. K. Schroeder, W. C. Duim, E. B. Kromann, T. Phan, F. E. Rivera-Molina, J. R. Myers, I. Irnov, M. Lessard, Y. Zhang, M. A. Handel, C. Jacobs-Wagner, C. P. Lusk, J. E. Rothman, D. Toomre, M. J. Booth, and J. Bewersdorf, Ultra-high resolution 3D imaging of whole cells, Cell **166**, 1028 (2016).

[11] A. Alva, E. Brito-Alarcón, A. Linares, E. Torres-García, H. O. Hernández, R. Pinto-Cámara, D. Martínez, P. Hernández-Herrera, R. D'Antuono, C. Wood, and A. Guerrero, Fluorescence fluctuation-based super-resolution microscopy: Basic concepts for an easy start, J. Microsc. **288**, 218 (2022).

[12] N. Gustafsson, S. Culley, G. Ashdown, D. M. Owen, P. M. Matos Pereira, and R. Henriques, Fast live-cell conventional fluorophore nanoscopy with ImageJ through super-resolution radial fluctuations, Nat. Commun. **7**, 12471 (2016).

[13] S. Munck, K. Miskiewicz, R. Sannerud, S. A. Menchon, L. Jose, R. Heintzmann, P. Verstreken, and W. Annaert, Sub-diffraction imaging on standard microscopes through photobleaching microscopy with non-linear processing, J. Cell Sci. **125**, 2257 (2012).

[14] A. Sroda, A. Makowski, R. Tenne, U. Rossman, G. Lubin, D. Oron, and R. Lapkiewicz, SOFISM: Super-resolution optical fluctuation image scanning microscopy, Optica **7**, 1308 (2020).

[15] M. G. L. Gustafsson, Nonlinear structured-illumination microscopy: Wide-field fluorescence imaging with theoretically unlimited resolution, Proc. Natl. Acad. Sci. USA **102**, 13081 (2005).

[16] F. Ströhl and C. F. Kaminski, Frontiers in structured illumination microscopy, Optica **3**, 667 (2016).

[17] I. J. Cox, C. J. R. Sheppard, and T. Wilson, Improvement in resolution by nearly confocal microscopy, Appl. Opt. **21**, 778 (1982).

[18] C. J. R. Sheppard, Super-resolution in confocal imaging, Optik (Stuttgart) **80**, 53 (1988).

[19] G. M. D. Luca, R. M. Breedijk, R. A. Brandt, C. H. Zeelenberg, B. E. de Jong, W. Timmermans, L. N. Azar, R. A. Hoebe, S. Stallinga, and E. M. Manders, Re-scan confocal microscopy: scanning twice for better resolution, Biomed. Opt. Express **4**, 2644 (2013).

[20] S. Roth, C. J. Sheppard, K. Wicker, and R. Heintzmann, Optical photon reassignment microscopy (OPRA), Opt. Nanoscopy **2**, 5 (2013).

[21] A. G. York, P. Chandris, D. D. Nogare, J. Head, P. Wawrzusin, R. S. Fischer, A. Chitnis, and H. Shroff, Instant super-resolution imaging in live cells and embryos via analog image processing, Nat. Methods **10**, 1122 (2013).

[22] A. G. York, S. H. Parekh, D. D. Nogare, R. S. Fischer, K. Temprine, M. Mione, A. B. Chitnis, C. A. Combs, and H. Shroff, Resolution doubling in live, multicellular organisms via multifocal structured illumination microscopy, Nat. Methods **9**, 749 (2012).

[23] S. V. Koho, E. Slenders, G. Tortarolo, M. Castello, M. Buttafava, F. Villa, E. Tcarenkova, M. Ameloot, P. Bianchini, C. J. R. Sheppard, A. Diaspro, A. Tosi, and G. Vicidomini, Two-photon image-scanning microscopy with spad array and

blind image reconstruction, Biomed. Opt. Express **11**, 2905 (2020).

[24] J. Huisken, J. Swoger, F. D. Bene, J. Wittbrodt, and E. H. K. Stelzer, Optical sectioning deep inside live embryos by selective plane illumination microscopy, Science **305**, 1007 (2004).

[25] P. W. Winter, A. G. York, D. D. Nogare, M. Ingaramo, R. Christensen, A. Chitnis, G. H. Patterson, and H. Shroff, Two-photon instant structured illumination microscopy improves the depth penetration of super-resolution imaging in thick scattering samples, Optica **1**, 181 (2014).

[26] I. Gregor, M. Spiecker, R. Petrovsky, J. Großhans, R. Ros, and J. Enderlein, Rapid nonlinear image scanning microscopy, Nat. Methods **14**, 1087 (2017).

[27] C. J. R. Sheppard, M. Castello, G. Tortarolo, G. Vicidomini, and A. Diaspro, Image formation in image scanning microscopy, including the case of two-photon excitation, J. Opt. Soc. Am. A **34**, 1339 (2017).

[28] C. J. R. Sheppard, M. Castello, G. Tortarolo, E. Slenders, T. Deguchi, S. V. Koho, G. Vicidomini, and A. Diaspro, Image scanning microscopy with multiphoton excitation or bessel beam illumination, J. Opt. Soc. Am. A **37**, 1639 (2020).

[29] N. G. Horton, K. Wang, D. Kobat, C. G. Clark, F. W. Wise, C. B. Schaffer, and C. Xu, *In vivo* three-photon microscopy of subcortical structures within an intact mouse brain, Nat. Photon. **7**, 205 (2013).

[30] K. Toda, K. Isobe, K. Namiki, H. Kawano, A. Miyawaki, and K. Midorikawa, Interferometric temporal focusing microscopy using three-photon excitation fluorescence, Biomed. Opt. Express **9**, 1510 (2018).

[31] C. J. R. Sheppard, Structured illumination microscopy and image scanning microscopy: a review and comparison of imaging properties, Philos. Trans. R. Soc. A **379**, 20200154 (2021).

[32] See Supplemental Material at http://link.aps.org/supplemental/10.1103/PRXLife.2.033010 for additional figures.

[33] I. L.-R. Qinggele Li and N. D. Lai, Influence of incident beam polarization on intensity and polarization distributions of tight focusing spot, Adv. Dev. Mater. **1**, 4 (2015).

[34] A. Fernandez, A. Classen, N. Josyula, J. T. Florence, A. Sokolov, M. O. Scully, P. Straight, and A. Verhoef, Simultaneous two- and three-photon deep imaging of autofluorescence in bacterial communities, Sensors **24**, 667 (2024).

[35] E. E. Diel, J. W. Lichtman, and D. S. Richardson, Tutorial: avoiding and correcting sample-induced spherical aberration artifacts in 3D fluorescence microscopy, Nat. Protocols **15**, 2773 (2020).

[36] R. Tenne, U. Rossman, B. Rephael, Y. Israel, A. Krupinski-Ptaszek, R. Lapkiewicz, Y. Silberberg, and D. Oron, Super-resolution enhancement by quantum image scanning microscopy, Nat. Photon. **13**, 116 (2019).

[37] G. Lubin, R. Tenne, I. M. Antolovic, E. Charbon, C. Bruschini, and D. Oron, Quantum correlation measurement with single photon avalanche diode arrays, Opt. Express **27**, 32863 (2019).

[38] A. C. Descloux, K. S. Grußmayer, V. Navikas, D. Mahecic, S. Manley, and A. Radenovic, Experimental combination of super-resolution optical fluctuation imaging with structured illumination microscopy for large fields-of-view, ACS Photon. **8**, 2440 (2021).

[39] Modular in vivo multiphoton microscopy system ((MIMMS) 1.0), https://www.janelia.org/open-science/mimms-10-2016, accessed: 2023-05-24.

[40] A. Fernández, A. Straw, M. Distel, R. Leitgeb, A. Baltuska, and A. J. Verhoef, Dynamic real-time subtraction of stray-light and background for multiphoton imaging, Biomed. Opt. Express **12**, 288 (2021).

[41] A. Fernández, L. Zhu, A. J. Verhoef, D. Sidorov-Biryukov, A. Pugžlys, A. Baltuška, K.-H. Liao, C.-H. Liu, A. Galvanauskas, S. Kane, R. Holzwarth, and F. O. Ilday, Broadly tunable carrier envelope phase stable optical parametric amplifier pumped by a monolithic ytterbium fiber amplifier, Opt. Lett. **34**, 2799 (2009).

[42] A. J. Verhoef, K. Jespersen, T. V. Andersen, L. Grüner-Nielsen, T. Flöry, L. Zhu, A. Baltuška, and A. Fernández, High peak-power monolithic femtosecond ytterbium fiber chirped pulse amplifier with a spliced-on hollow core fiber compressor, Opt. Express **22**, 16759 (2014).

[43] F. L. Jalufka, S. W. Min, M. E. Platt, A. L. Pritchard, T. E. Margo, A. O. Vernino, M. A. Kirchhoff, R. T. Massopust, and D. A. McCreedy, Hydrophobic and hydrogel-based methods for passive tissue clearing, in *Fluorescent Microscopy*, edited by B. Heit (Springer US, New York, 2022), pp. 197–209.

[44] D. Sage, L. Donati, F. Soulez, D. Fortun, G. Schmit, A. Seitz, R. Guiet, C. Vonesch, and M. Unser, Deconvolutionlab2: An open-source software for deconvolution microscopy, Methods **115**, 28 (2017).